

Article

The Combined Impact of Ni-Based Catalysts and a Binary Carbonate Salts Mixture on the CO₂ Gasification Performance of Olive Kernel Biomass Fuel

Athanasios Lampropoulos ^{1,*}, Stamatia A. Karakoulia ², Georgios Varvoutis ¹, Stavros Spyridakos ¹, Vassilios Binas ³, Leila Zouridi ^{3,4}, Sofia Stefa ⁵, Michalis Konsolakis ⁵ and George E. Marnellos ^{1,2,*}

¹ Department of Mechanical Engineering, University of Western Macedonia, 50100 Kozani, Greece

² Chemical Process and Energy Resources Institute, Centre for Research and Technology Hellas, 57001 Thessaloniki, Greece

³ Institute of Electronic Structure and Laser, Foundation for Research and Technology-Hellas, 70013 Heraklion, Greece

⁴ Department of Material Science and Technology, University of Crete, 71003 Heraklion, Greece

⁵ School of Production Engineering and Management Technical, University of Crete, 73100 Chania, Greece

* Correspondence: alabropoulos@uowm.gr (A.L.); gmarnellos@uowm.gr (G.E.M.);

Tel.: +30-24610-56702 (A.L.); +30-24610-56690 (G.E.M.)

Abstract: In the present work, the individual or synergistic effect of Ni-based catalysts (Ni/CeO₂, Ni/Al₂O₃) and an eutectic carbonate salt mixture (MS) on the CO₂ gasification performance of olive kernels was investigated. It was found that the Ni/CeO₂ catalyst presented a relatively superior instant gasification reaction rate (R_{co}) compared to Ni/Al₂O₃, in line with the significant redox capability of CeO₂. On the other hand, the use of the binary eutectic carbonate salt mixture (MS) lowered the onset and maximum CO₂ gasification temperatures, resulting in a notably higher carbon conversion efficiency (81%) compared to the individual Ni-based catalysts and non-catalytic gasification tests (60%). Interestingly, a synergetic catalyst-carbonate salt mixture effect was revealed in the low and intermediate CO₂ gasification temperature regimes, boosting the instant gasification reaction rate (R_{co}). In fact, in the temperature range of 300 to 550 °C, the maximum R_{co} value for both MS-Ni/Al₂O₃ and MS-Ni/CeO₂ systems were four times higher ($4 \times 10^{-3} \text{ min}^{-1}$ at 460 °C) compared to the individual counterparts. The present results demonstrated for the first time the combined effect of two different Ni-based catalysts and an eutectic carbonate salt mixture towards enhancing the CO production rate during CO₂ gasification of olive kernel biomass fuel, especially in the devolatilization and tar cracking/reforming zones. On the basis of a systematic characterization study and lab-scale gasification experiments, the beneficial role of catalysts and molten carbonate salts on the gasification process was revealed, which can be ascribed to the catalytic activity as well as the improved mass and heat transport properties offered by the molten carbonate salts.



Citation: Lampropoulos, A.; Karakoulia, S.A.; Varvoutis, G.; Spyridakos, S.; Binas, V.; Zouridi, L.; Stefa, S.; Konsolakis, M.; Marnellos, G.E. The Combined Impact of Ni-Based Catalysts and a Binary Carbonate Salts Mixture on the CO₂ Gasification Performance of Olive Kernel Biomass Fuel. *Catalysts* **2023**, *13*, 596. <https://doi.org/10.3390/catal13030596>

Academic Editor: Georgios Bampos

Received: 12 February 2023

Revised: 10 March 2023

Accepted: 13 March 2023

Published: 16 March 2023

Keywords: olive kernel; CO₂ gasification; Ni/CeO₂; Ni/Al₂O₃; molten carbonates salt (MS); instant gasification rate; carbon conversion



Copyright: © 2023 by the authors. Licensee MDPI, Basel, Switzerland. This article is an open access article distributed under the terms and conditions of the Creative Commons Attribution (CC BY) license (<https://creativecommons.org/licenses/by/4.0/>).

1. Introduction

The increasing demand for more energy worldwide, along with the rising concerns on climate change, are forcing humanity to speed up defossilization and prioritize the clean transition of the energy mix [1]. However, the wide deployment of intermittent renewables, such as solar and wind power, requires the development of energy and cost efficient large-scale seasonal energy storage technologies to balance electricity grids and avoid costly curtailments, which has not yet been convincingly achieved nowadays [2]. On the other hand, if logistics are resolved, the use of bioenergy potential could sufficiently meet the energy demand and decarbonize our economies. In specific, the thermochemical

exploitation of biomass (combustion, pyrolysis, gasification, etc.) is expected to notably suppress greenhouse gas (GHG) emissions due to the carbon neutral nature of biomass [1,3,4]. According to Di Gulliano et al. [5], biomass-based power plants accompanied by CO₂ capture can achieve negative CO₂ emissions, leading to an estimated CO₂ sequestration potential of 2.0–12.0 Gt CO₂ by 2050.

Agricultural and agro-industrial activities are the main sources of residual biomass that could be used as renewable feedstock in thermochemical cycles, thus enhancing local economies and minimizing waste handling problems [6–10]. Greece possesses large quantities of animal manure and agricultural and agro-industrial residues that are equal to 50 Mt/year [11]. Olive oil industry residues (tree pruning, leaves, pits, kernel and pomace) represent 20% of the total annual residual biomass in Greece, which is the third largest olive oil industry worldwide (350 ktons/year) [12,13]. Specifically, olive kernel accounts for 15% of the total residues resulting as by-products from the olive oil extraction process [14,15]. Among other residues, olive kernel exhibits the lowest moisture content (5–15%), and is thus considered a saleable fuel without further treatment [14–16]. Assuming an average lower heating value (LHV) of olive-based biomass residues equal to 16–18 MJ/kg [17–21] and an electrical efficiency of 25–35% [22–24], the thermochemical exploitation of the total annual quantity of olive oil-industry residues in Greece (10 Mt) could potentially produce around 14–15 GWh/year of energy. However, uncertainties associated with the Greek institutional framework towards biomass-based power plants are slowing down practical applications at larger scales [25–27].

Converting biomass to heat, electrical power, biofuels, and chemicals via the gasification process is of paramount importance in achieving energy independence and increasing the share of renewables in the energy mix. In principle, gasification process includes two main consecutive steps: (a) a relatively fast step ($t < 60$ s @ 300–700 °C), involving the thermal decomposition of volatile components to gaseous products, tars (condensable hydrocarbon compounds), and a solid char residue, and (b) a slower step ($t > 3300$ s @ $T > 700$ °C), including the gasification of the pyrolyzed char (gas-solid reactions) along with other gas-phase reforming reactions [28]. Suitable gasifying agents (air, steam, CO₂, or their mixture) can benefit the gasification reaction of the remaining char [4,29,30]. Apart from the gasifying agent, from a process system perspective, the main factors affecting syngas quality and quantity are the employed operating temperature and pressure, gasifier design and heating mode, the addition of catalysts, and the feedstock composition [31,32].

Despite the advantages of biomass exploitation through the gasification process, there are specific challenges that seriously affect the gasification performance in terms of the as-produced syngas quantity and quality. Syngas clean-up from impurities such as tars and water is of high priority towards producing a final product suitable for several downstream processes, i.e., in high-temperature fuel cells for the co-generation of heat and power or in catalytic reactors for the production of synthetic fuels and/or chemicals [33–35]. Mechanical separation methods for the removal of particulate matter (wet scrubber, cyclone, filter, and electrostatic precipitator), along with tar thermal cracking, have been widely used for syngas clean-up and conditioning [36–38]. However, the relatively high capital cost and the formation of small, complex tar structures restrict the commercialization of gasification technology [38]. In this regard, the use of highly active catalysts, in situ or outside the gasifier, has been proposed to reform tars, generating additional syngas with negligible impurities. Moreover, the use of catalysts in gasification leads to faster kinetics at decreased temperatures, further enhancing its efficiency [33,34,39]. Numerous studies [40–43] highlighted the main criteria for a good catalyst selection, which include the decrease of energy activation for tar cracking, gas-solid and gas-phase reactions, the reduced supply of gasifying agents, and the generation of high-value chemicals.

In general, catalysts used in biomass gasification can be divided into three major categories: (a) natural mineral catalysts (dolomite, olivine, zeolites, alumina), (b) alkali and alkaline Earth metal catalysts, AAEMs (Li, Na, K, Mg, Ca, and Rb), and (c) transition metal catalysts [44,45]. Among all of the transition metals (group VIII), Ni-based catalysts

have been widely reported in the literature [28,44,46–50]. This can be attributed to their remarkable role on tar removal, steam reforming, and water gas shift (WGS) reactions, for H₂-rich syngas production [44,45]. For instance, Baker et al. [51] and Li et al. [52] investigated the performance of commercial nickel catalysts in fluidized bed gasifiers in the temperature range of 700–800 °C during sawdust and pine flakes steam gasification. They both noticed the pronounced role of Ni catalysts during steam gasification in terms of gaseous product yield and tar elimination. However, in both studies, the catalysts suffered from rapid deactivation (<5 h) due to carbon deposition on the catalyst surface and nickel particles sintering. In this regard, numerous studies investigated and proposed alternative routes to modify Ni based catalysts, including the use of different supporting materials and/or aliovalent doping (Fe, Co, La Ce, Mg, etc.) [46–50,53–62]. Several types of supporting materials have been examined in the literature, involving metal oxides, among others [44,45]. Metal oxides (CeO₂, Al₂O₃, ZrO₂), natural minerals (olivine, dolomite), and zeolites can provide mechanical strength, improved textural properties, and adsorption ability if they are employed as supports in Ni-based catalysts [63,64].

In addition to the use of catalysts, molten alkali carbonate (MAC) salts have been extensively studied in biomass gasification for tar elimination and enhanced syngas production [65–67]. In general, MAC salts (Li₂CO₃, Na₂CO₃, K₂CO₃, etc.) in eutectic compositions can be utilized as excellent industrial fluids in a wide range of high temperature operating technologies (solar power applications, waste oxidation, direct carbon fuel cells, and catalytic biomass gasification) [66]. A well-established application of MAC salts is as heating carriers, since they exhibit a dual function as solar heat storage and heat transfer media [65]. Unlike the use of solar-heated MACs as an indirect heating medium for pyrolysis and/or gasification processes, the direct contact of molten salts and biomass particles can lead to an enhanced gasification rate and syngas production. This enhancement can be attributed to the facilitation of mass and heat transfer phenomena induced by MACs in conjunction with their alkali-based catalytic nature [66].

Various studies have been devoted to interpreting the gasification mechanism of solid fuels in the presence of MAC salts [68–74]. Notably, the majority of works are dealing with pure carbon and coal/biomass chars. For instance, Mckee and co-investigators [68] concluded that the catalytic gasification of coal char over K₂CO₃ involves the following steps: (a) melting of K₂CO₃ salt, (b) its precipitation at the char surface area (pores), and (c) the formation of a thin layer favoring the carbon-catalyst interaction.

Gasifying agents notably affect the overall reaction network and, in turn, the syngas formation reaction rate. Strong gasifying agents (pure oxygen and steam) can affect the thermal stability of MAC salts [75], whereas the formation of hydroxide intermediates (MOH) and salt oxides (M₂O₂) may lead to fouling and plugging of the reactor and pipeline system [28,76]. However, CO₂ is expected to be a suitable gasifying agent for biomass gasification in the presence of MAC catalysts since it can maintain MACs' stability at high temperatures [28]. Taking into account the efforts towards CO₂ mitigation, CO₂ biomass gasification over MAC salts can be a promising route towards producing biofuels and high value products with negative CO₂ emissions [77–80]. In the light of the above aspects, the majority of the studies regarding biomass gasification over MAC salts are restricted to the use of CO₂ as a gasifying agent [28,81–87].

As mentioned above, the char-CO₂ gasification reaction requires more energy compared to other gasifying agents (air, oxygen, and steam) and can be considered the rate-determining step of the overall reaction network [88]. Interestingly, catalyst addition to MACs could synergistically lead to enhanced tar-free syngas production, sufficiently simplify gas clean-up steps, and render the whole process less complex and economically feasible for large-scale applications [28]. As extensively mentioned above, commercial nickel and modified Ni-based catalysts can facilitate biomass gasification, tar cracking, and reforming reactions. In fact, Ni-based catalysts are both selective for hydrogen production and highly efficient towards carbon conversion. Very few works have reported on the combination of Ni-based catalysts and molten alkali carbonate salts during biomass

gasification [28,76]. Specifically, Sakhon Ratchahat and co-workers [28,76] investigated the catalytic effect of a combined Ni/Al₂O₃ and ternary carbonate salt (Li₂-K₂-Na₂-CO₃) catalytic system on the pyrolysis and CO₂ gasification of different biomass wastes.

In this context, the present work aims for the first time to systematically explore the combined impact of different Ni-based catalysts (Ni/CeO₂ and Ni/Al₂O₃) and an eutectic binary carbonate salt mixture (Li₂CO₃-K₂CO₃ molten salt, MS) on the CO₂ gasification performance of olive kernels under non-isothermal operating conditions in a lab-scale fixed-bed reactor. Various characterization techniques (H₂-TPR, SEM, HR/SEM_EDS, TEM, HR/TEM, and XRD) were applied to investigate the morphological and structural properties of these catalysts. It was disclosed that the type of commercial metal oxide used as support (Al₂O₃ or CeO₂) does not significantly affect the activity of Ni catalysts towards CO₂ gasification. However, the addition of the binary eutectic carbonate mixture (MS) resulted in a notably favorable performance during olive kernel-CO₂ gasification tests, leading to a high CO yield and carbon conversion efficiency. More interestingly, a synergistic MS-Ni medium effect in the low-temperature CO₂ gasification zone was revealed, boosting carbon monoxide production yields and carbon conversion efficiency.

2. Results and Discussion

2.1. Structural Characterization (XRD Analysis)

Figure 1 shows the XRD patterns of Ni/CeO₂, Ni/Al₂O₃ and their blends with the binary carbonate salt mixture. All catalysts exhibited the characteristic peaks of cubic NiO at 2θ angles of ca. 37, 43, 63, 76, and 79.5° (PDF #73-1519). No characteristic peaks of precursor Ni(NO₃)₃ or of other nitrates were detected, indicating that nickel nitrate was totally utilized and decomposed during the catalysts' preparation procedure. Furthermore, the d-spacing (d) values of as-prepared catalysts, calculated by Bragg's law, along with the corresponding lattice parameters (α), are summarized in Table 1. In addition, by applying the Scherrer equation [89], the primary crystallite sizes (D_{XRD}) of ceria and alumina were found to be 54.92 and 73.22 nm, respectively (Table 1). Moreover, the crystallite size (D_{XRD}) of the NiO particles on both the alumina and ceria supports was calculated at ca. 40 nm (37.22 and 42.83, respectively, in Table 1), in accordance with HR-SEM observations (Section 2.2). Both MS-Ni catalysts exhibited characteristic peaks at 2θ angles of 28–35, 40, and 47°, which are attributed to Li₂CO₃-K₂CO₃ carbonates (Figure 1).

Notably, the characteristic peaks attributed to NiO and carbonates phases present lower intensities in the case of CeO₂-containing samples, ascribed to the higher crystallinity of ceria compared to that of alumina. However, in the case of Ni/Al and MS-Ni/Al catalysts, the high-intensity characteristic peaks at 2θ = 37 and 43° can be ascribed to the co-existence of NiO, Al₂O₃, NiAl₂O₄ and carbonates phases. Interestingly, it should be noticed that small shoulder peaks standing for NiAl₂O₄ spinel oxide (#77-1877) can be found at 2θ = 37, 45, and 65°, indicating its formation, which has also been confirmed by H₂-TPR (see in Section 2.3). In particular, under high calcination temperatures (above 700 °C), nickel ions are migrating into the alumina lattice, forming the spinel structure (NiAl₂O₄), through the solid-solid interaction of NiO with Al₂O₃.

2.2. Morphological Characterization (SEM, HR-SEM, EDS Mapping, and TEM)

Figure 2 illustrates the SEM images of the fresh samples prior to gasification experiments. It can be observed from Figure 2a,b that both Ni/Al₂O₃ and Ni/CeO₂ catalysts display an irregular morphology consisting of nano-sized particles. Additionally, micro-scaled agglomerates are present on both catalysts, attributed to the high calcination temperature, which presumably leads to the sintering of NiO particles and/or supporting materials [44,45].

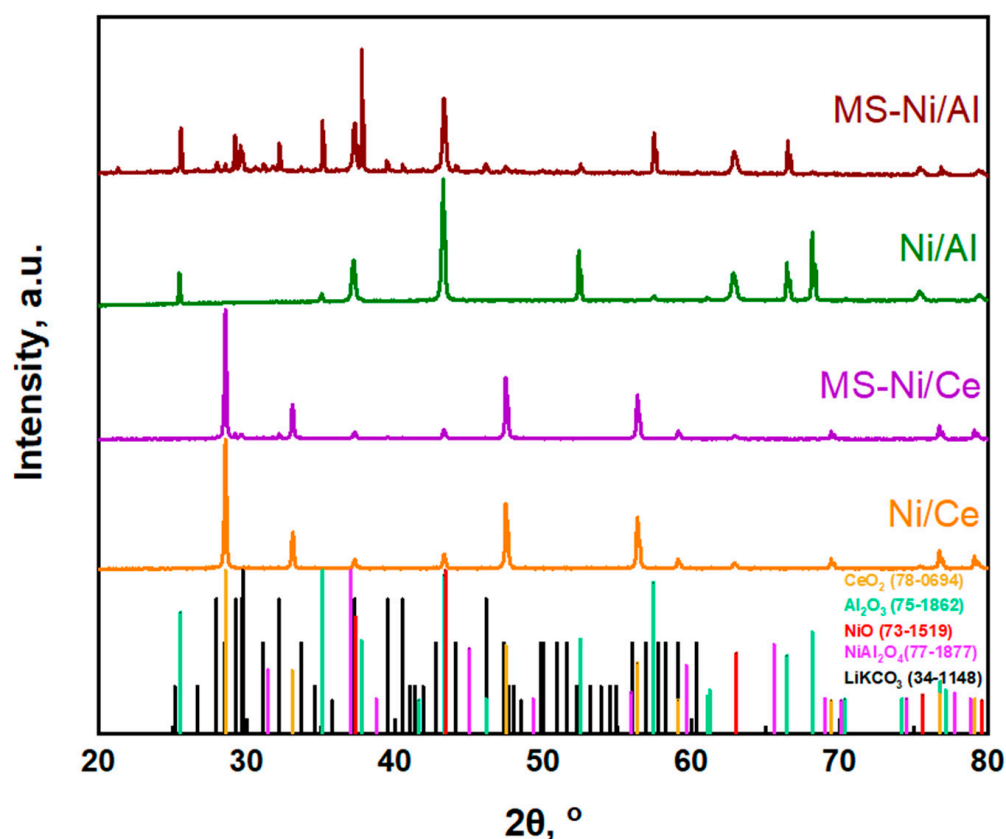


Figure 1. XRD patterns of Ni-based and MS-Ni-based catalysts.

Table 1. XRD and TEM results for the as-prepared Ni/CeO₂ and Ni/Al₂O₃ catalysts.

Sample	XRD						TEM
Ni/CeO ₂	CeO ₂ (111)			NiO (200)			NiO mean particle size
	D _{XRD} (nm) ¹	d (nm) ²	a (nm)	D _{XRD} (nm) ¹	d (nm) ²	a (nm)	38.1 ± 8.5
	54.92	0.31	0.54	42.83	0.21	0.42	
Ni/Al ₂ O ₃	Al ₂ O ₃ (113)			NiO (200)			NiO mean particle size
	D _{XRD} (nm) ¹	d (nm) ²	a (nm)	D _{XRD} (nm) ¹	d (nm) ²	a (nm)	37.7 ± 9.0
	73.22	0.21	n/a*	37.22	0.21	0.42	

* Aluminum forms a rhombohedral crystal lattice, not a cubic lattice such as CeO₂ and NiO. ¹ Calculated applying Scherrer's equation. ² Calculated by Bragg's law.

Figure 2c illustrates a uniform surface for the binary molten salt carbonate mixture (MS) with particle sizes less than 10 μm, confirming that the preparation protocol resulted in a relatively homogeneous blend. In the case of MS/catalyst mixtures (Figure 2d,e), the catalytic particles retained their irregular shape together with the presence of certain agglomerates due to the calcination pretreatment. At the same time, EDS analysis (not shown for the sake of brevity) demonstrates that Ni loading is practically equal to the nominal one (ca. 15 wt.%) in the case of Ni/CeO₂, whereas a slightly lower value was revealed for Ni/Al₂O₃ (13 wt.%).

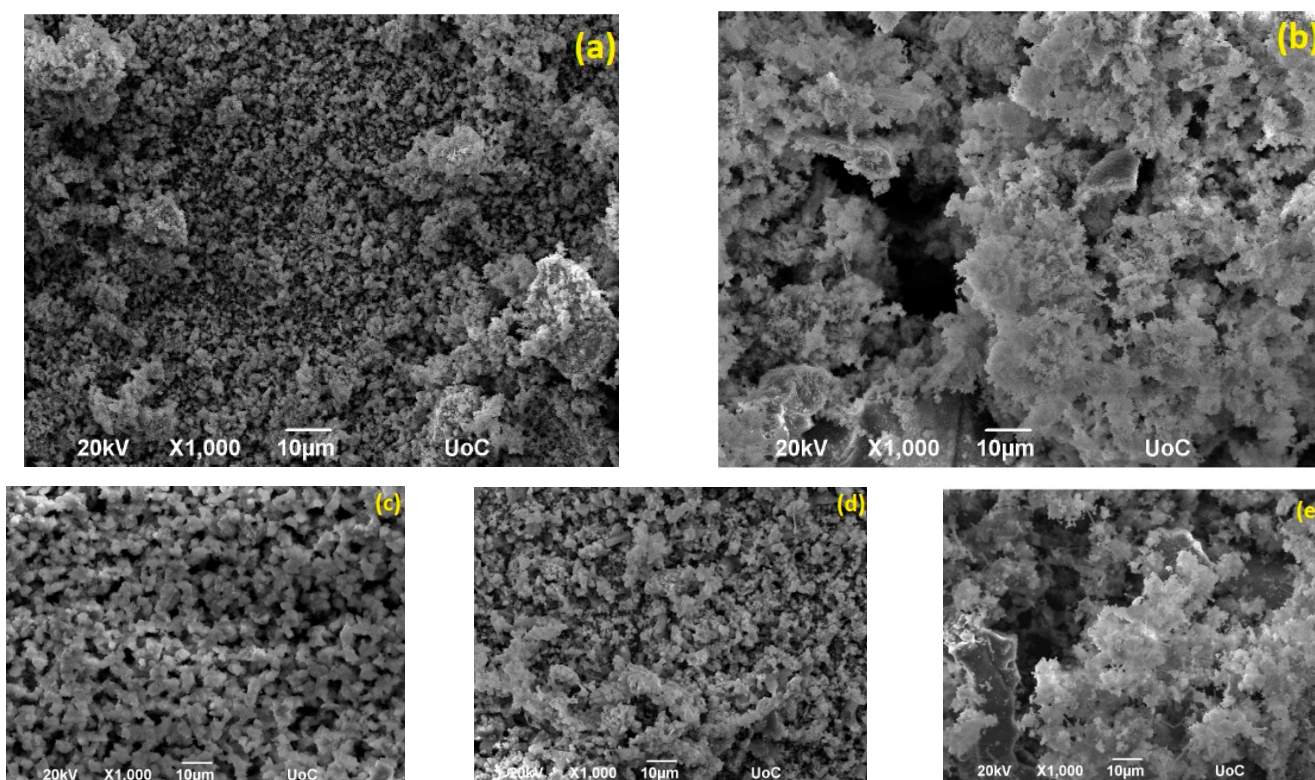


Figure 2. SEM images of the as-prepared samples: (a) Ni/CeO₂; (b) Ni/Al₂O₃; (c) MS (d) MS-Ni/CeO₂; and (e) MS-Ni/Al₂O₃.

TEM analysis was applied to gain further insight into the morphological features of the samples (Figure 3). The bare support materials are presented in Figure 3a,b, while Ni/CeO₂ and Ni/Al₂O₃ are shown in Figure 3c,d. In the case of both Ni/CeO₂ and Ni/Al₂O₃, the mean particle size of NiO was ca. 40 nm, verifying the XRD findings, as shown in Table 1. It is worth noting that the wet-impregnation method and calcination at 850 °C resulted in similar NiO particle sizes. Given the inherent difficulties in distinguishing between commercial CeO₂ and NiO particles, the lattice fringes of NiO and CeO₂ were identified, which are reflective of the crystallinity of the samples. In particular, for the Ni/CeO₂ sample, the distinction was established by the calculation of the d-spacing values in an indicative HR-TEM image (Figure 3e). The lattice spacing for the phases of NiO and CeO₂ were 0.2 and 0.3 nm, respectively, which confirms the presence of NiO particles by exposing (200) planes that are in contact with CeO₂ (111), further confirming the results from XRD. In addition, it can be clearly seen that NiO cluster particles are semi-submerged upon the CeO₂ support and are characterized by a quasi-spherical shape.

2.3. Redox Behavior (H₂-TPR Analysis)

The reduction profiles (H₂-TPR) of Ni/CeO₂ and Ni/Al₂O₃ samples are compared in Figure 4. Four major H₂ consumption peaks were observed for both Ni-based catalysts. Notably, for Ni/CeO₂, the onset reduction temperature is around 180 °C, whereas for Ni/Al₂O₃, this temperature is significantly higher (ca. 235 °C), implying the beneficial effect of ceria in the low-temperature reducibility [58,90–92]. Specifically, a low-temperature peak at 295 °C (peak α) and a prominent medium-temperature peak at 376 °C (peak β) can be distinguished in the low-temperature region (below 500 °C) for the Ni/CeO₂ catalyst. These peaks can be associated with the reduction of NiO species strongly interacting with the CeO₂ support [46,50,91,93–96]. Notably, a shoulder at 242 °C can be in addition observed, which can be ascribed to the reduction of the loosely bound NiO species and/or to surface-absorbed O²⁻/O⁻ species (oxygen vacancies associated with the formation of the Ni-O-Ce structure) [97,98]. The peak at 502 °C (peak γ) corresponds to the reduction of

bulk NiO species. Lastly, the low intensity reduction peak above 750 °C (peak δ) can be attributed to the reduction of the CeO₂ bulk [46,50,91,93]. For the Ni/Al₂O₃ catalyst, one smaller and two major reduction peaks were observed at 310, 436, and 507 °C, respectively. The first peak (peak α) is assigned to the reduction of the loosely bound NiO species, whereas the two peaks at 436 and 507 °C (peaks β , γ) are attributed to the NiO species interacting with the Al₂O₃ support [91–93]. Finally, the last reduction feature (peak δ) at the high temperature zone (above 900 °C) corresponds to the reduction of NiAl₂O₄ spinel phases, suggesting a strong interaction between NiO and Al₂O₃ species, in good agreement with the XRD findings and relevant literature studies [50,91,93,97,98].

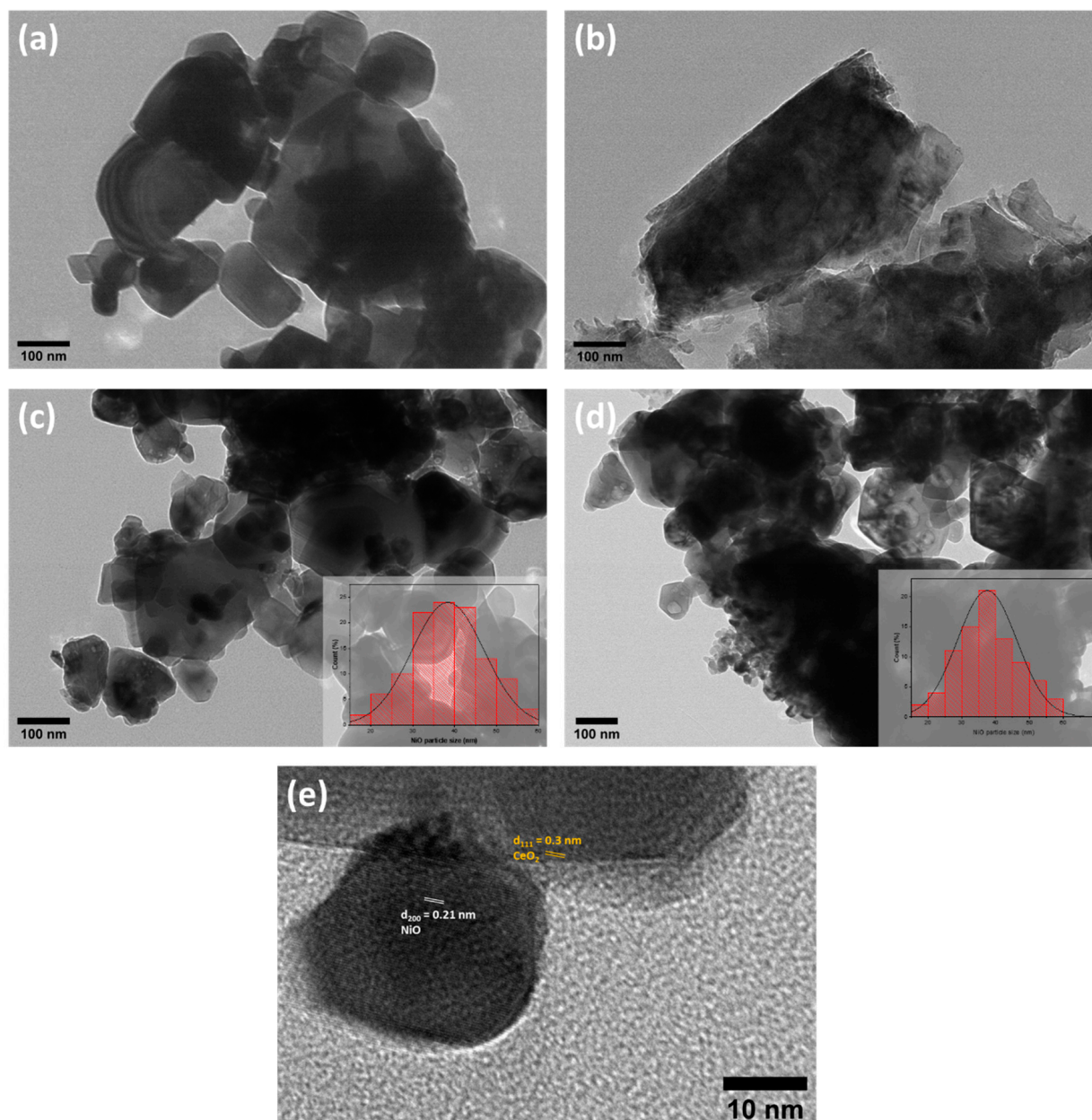


Figure 3. (a) TEM image of CeO₂; (b) TEM image of Al₂O₃; (c,d) TEM images and NiO particle size distribution (PSD histograms) of the as-prepared Ni/CeO₂ and Ni/Al₂O₃, respectively; (e) HRTEM image of Ni/CeO₂.

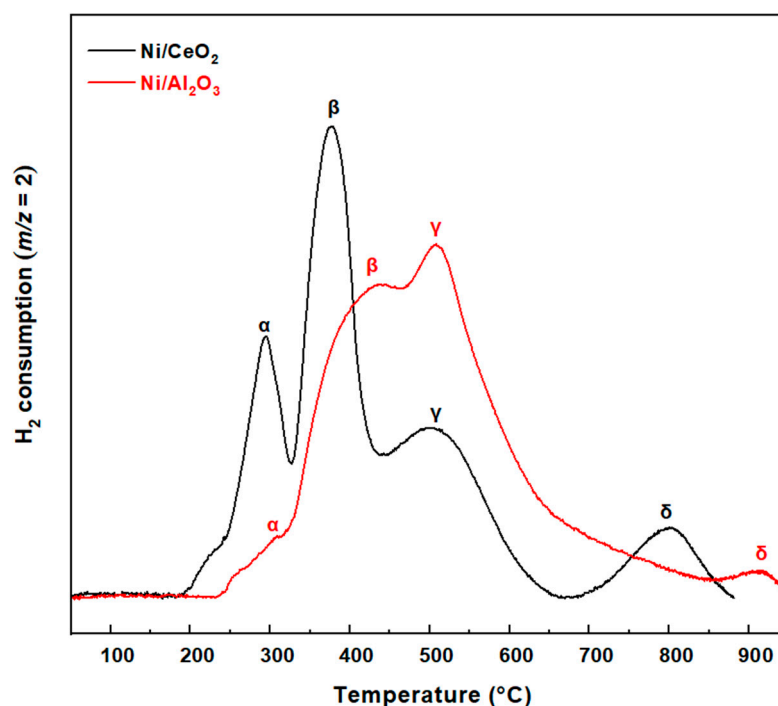


Figure 4. H₂-TPR profiles of the as-prepared Ni/CeO₂ and Ni/Al₂O₃ catalysts.

Quantitative analysis of the H₂-TPR profiles was also carried out by calculating the H₂ uptake (mmol H₂/g) of each peak (Table 2). As expected, regarding the reducibility of the samples in the low-temperature region ($T < 500$ °C), the calculated H₂ consumption values were almost identical for both Ni/CeO₂ and Ni/Al₂O₃ catalysts (2.5 mmol/g_{cat}). However, H₂ is consumed at relatively lower temperatures in the case of the Ni/CeO₂ catalyst, indicative of the superior reducibility of ceria-based oxides, facilitated by metal-support interactions [46,90,97,99]. Moreover, the total hydrogen consumption in the case of Ni/Al₂O₃ catalyst (2.65 mmol H₂/g_{cat}), which almost coincides with the theoretical amount of H₂ required for the complete reduction of NiO to metallic Ni⁰ (~2.5 mmol H₂/g_{cat}), implies a complete reduction of NiO species. On the other hand, in the case of the Ni/CeO₂ catalyst, the relatively higher H₂ consumption (compared to the theoretical one) can be presumably attributed to the reduction of surface oxygen species of CeO₂, which is facilitated by nickel-ceria interactions. To summarize, the results show that both Ni catalysts present a redox ability at the lower (250–400 °C) and intermediate (400–600 °C) temperature regimes. This can be an indication that more labile oxygen species could be involved in the primary and secondary tar cracking and/or reforming reactions, effectively reducing the tar content in the as-produced syngas [100]. Moreover, the peak observed at 800 °C and attributed to the reduction of bulk CeO₂ species may lead to additional syngas production by the oxidation of the remaining char and/or formatted carbon on the catalyst's surface (carbon deposition) [99].

Table 2. Redox properties of the Ni/CeO₂ and Ni/Al₂O₃ samples.

	Total H ₂ Uptake (mmol H ₂ /g)	α	β	γ	δ
Ni/CeO ₂	2.85	0.69 (295 °C)	1.10 (376 °C)	0.70 (502 °C)	0.35 (802 °C)
Ni/Al ₂ O ₃	2.65	0.04 (310 °C)	1.33 (436 °C)	1.21 (507 °C)	0.06 (916 °C)

2.4. Catalyst-Aided CO₂ Gasification Experiments under Batch Mode of Operation

Figures 5 and 6 depict the instant CO production rate, R_{CO} (min⁻¹), and carbon to CO conversion efficiency, X_{CO} , as a function of temperature during the batch non-isothermal

CO₂ catalytic gasification tests over the different catalytic systems examined (Ni/CeO₂, Ni/Al₂O₃, MS, and MS-Ni systems). For comparison purposes, the catalyst-free gasification experiments are also included. The CO₂ gasification process includes two consecutive steps (Table 3): the volatile decomposition and tar cracking/reforming reactions (R1-R6,) in the temperature range of 300–600 °C (step 1), and the reaction of the remaining char with CO₂ (R9) along with other solid and/or gas-phase reactions (R7, R8), denoted as step 2 [36].

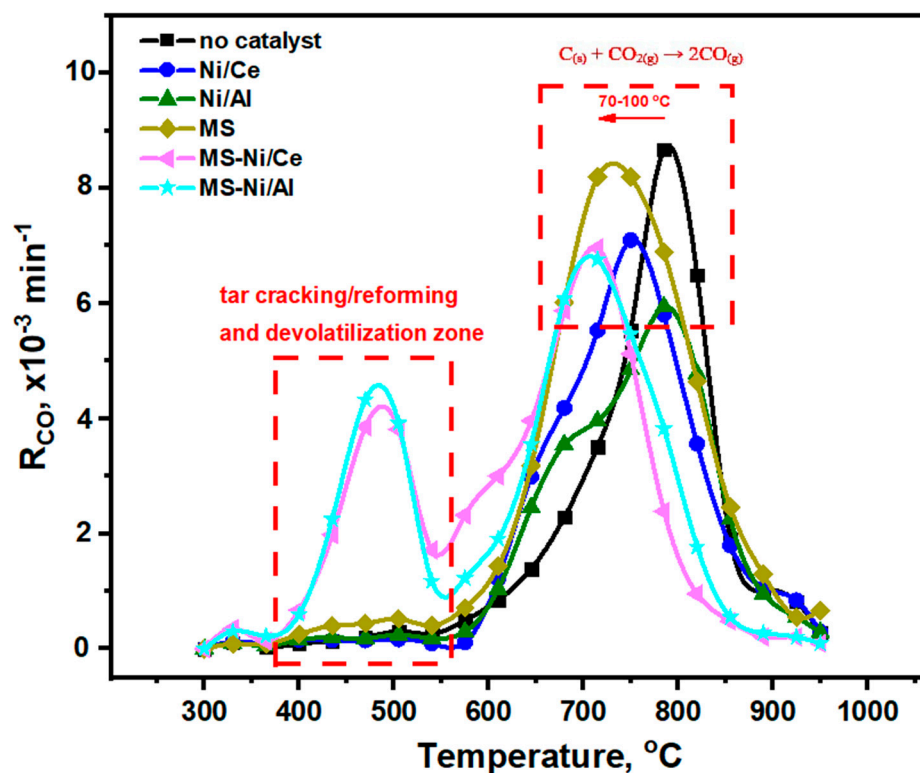


Figure 5. Effect of temperature and catalyst addition on the instant CO production rate (R_{CO}) during non-isothermal CO₂ gasification experiments. Gasifying agent flowrate = 30 cm³/min of 20 vol.% CO₂ in Helium.

In this regard, X_{CO} (Equation (1) in Section 3.4) involves a first term standing for the CO production during the tar cracking and devolatilization stage and a second term corresponding to the CO formation associated with the Boudouard reaction (R9) during the gasification stage [81,101]. In all cases, carbon monoxide was the principal product of gasification, appearing at different temperature regimes depending on the presence and the of catalyst. CO production, which is favored with temperature due to the endothermic reaction R9 [77], reaches its maximum and then gradually decreases until fuel depletion. During the olive kernel non-catalytic CO₂ gasification, a maximum R_{CO} value ($8.5 \times 10^{-3} \text{ min}^{-1}$) was observed at a temperature of 785 °C. Both Ni/CeO₂ and Ni/Al₂O₃ catalysts did not reveal any significant effect on the CO production rate. However, a slight reduction in the onset and peak gasification temperature was noticed in the case of the Ni/CeO₂ catalyst. Indeed, the maximum R_{CO} value for Ni/CeO₂ sample (ca. $7 \times 10^{-3} \text{ min}^{-1}$) was attained at 750 °C, which is 35 °C lower compared to the non-catalytic gasification. On the other hand, Ni/Al₂O₃ exhibited a maximum R_{CO} value equal to $6 \times 10^{-3} \text{ min}^{-1}$ at 780 °C, a slightly lower temperature compared to the un-catalyzed reaction (795 °C). The lower R_{CO} values obtained during the Ni-based catalytic CO₂ gasification reaction as compared to the non-catalytic process ($8.5 \times 10^{-3} \text{ min}^{-1}$) can possibly be attributed to the faster fuel depletion in conjunction with the favorable conditions for the endothermic Boudouard reaction (R9), since the gasification process takes place at lower temperatures. However, in the temperature regime of 600–750 °C, the R_{CO} values for the Ni-based catalysts were higher compared to those obtained during the uncatalyzed gasification reaction. Apart from the

CO generated via the endothermic R9 reaction, Sakhon Ratchahat and co-investigators [28] proposed a different pathway for CO production. In brief, solid carbon atoms react with the adsorbed oxygen on a support surface, resulting from the CO₂ dissociation on Ni active sites, leading to additional CO production (carbon cleavage reaction on Ni active sites). Notably, for the Ni/Al₂O₃ catalytic gasification, at temperatures above 650–700 °C, the R_{co} values present a pronounced descending trend compared to the Ni/CeO₂ catalyst. This can presumably be attributed to two different phenomena that take place during the high temperature char-gasification stage: (a) the inhibiting role of NiAl₂O₄ spinel species observed in XRD and H₂-TPR tests on catalytic gasification performance [102–104], and (b) the coke/carbon formation through the thermal and catalytic decomposition of carbonaceous intermediates and/or undesired gas phase side reactions. Indeed, since NiAl₂O₄ cannot be easily reduced to Ni⁰, its formation probably lowers the amount of active Ni sites, thus leading to a reduced catalytic activity [102]. On the other hand, a superior gasification rate is observed for Ni/CeO₂ sample up to 800 °C, which can be related to the high catalytic activity of Ni/CeO₂ catalyst and its tolerance toward carbon formation. CeO₂-based catalysts present a significant redox ability by releasing and up-taking oxygen through the reversible reaction, CeO₂ ↔ CeO_{2-x} + O_x, where O_x stands for the lattice oxygen at CeO₂ [33,34]. This lattice oxygen possibly enhances the catalytic gasification performance via two different pathways. The first one is by the reaction of CO with CeO₂ lattice oxygen, resulting in CO₂ formation (CO + O_x → CO₂ + O_{x-1}). The second one is related to the oxidation of the remaining solid char/carbon which could be facilitated by CeO₂. Indeed, as a supplier of lattice oxygen, CeO₂ may oxidize solid carbon (C_(s) + O_x → CO + O_{x-1}) towards additional CO formation. These induced effects are in line with the enhanced Ni/CeO₂ reducibility results (Figure 4, Table 2); the peak observed at 800 °C and attributed to the reduction of bulk CeO₂ species confirms the presence of lattice oxygen at such high temperatures, which can further oxidize the remaining carbon species [99].

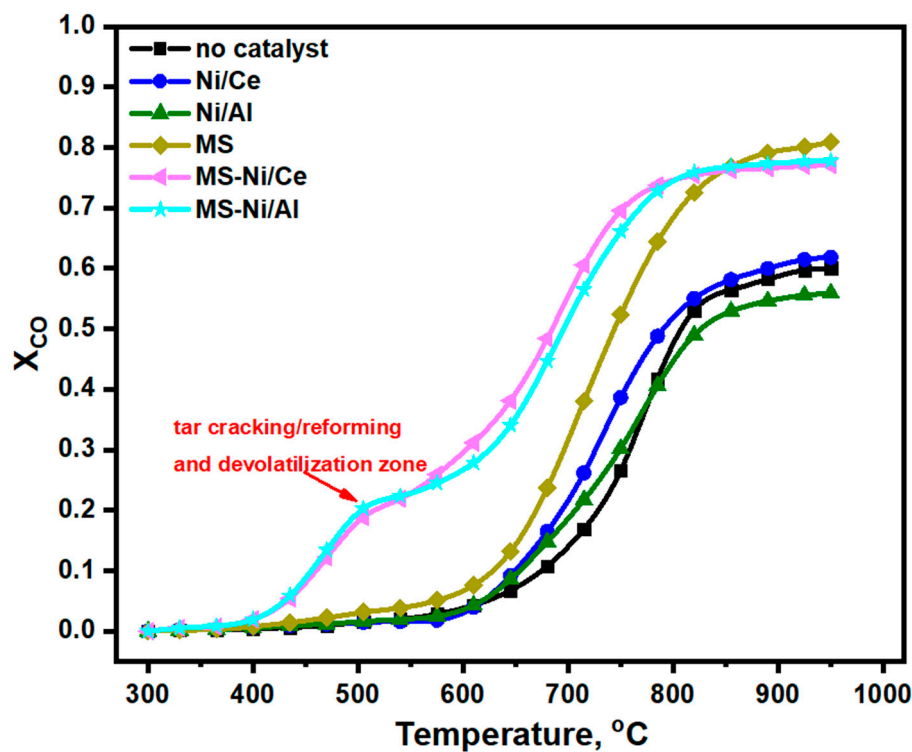


Figure 6. Effect of temperature and catalyst addition on the conversion of carbon to CO during non-isothermal CO₂ gasification experiments. Gasifying agent flowrate = 30 cm³/min of 20 vol.% CO₂ in Helium.

Table 3. The main reaction network during biomass CO₂ gasification.

	Reaction	No
Tar thermal cracking	Tar (C _m H _n) → Smaller Tar (C _q H _q) + H _{2(g)}	R1
Tar dry reforming	Tar (C _m H _n) + mCO _{2(g)} → 2mCO _{2(g)} + (n/2)H _{2(g)}	R2
Tar dry reforming	Tar (C _m H _n) + (m + n/2)CO _{2(g)} → (2m + n/2)CO _(g) + (n/2)H _{2(g)}	R3
Tar steam cracking	Tar (C _m H _n) + mH _{2O(g)} → mCO _(g) + (m + n/2)H _{2(g)}	R4
Tar steam cracking	Tar (C _m H _n) + 2mH _{2O(g)} → mCO _{2(g)} + (2m + n/2)H _{2(g)}	R5
Tar partial oxidation	Tar (C _m H _n) + (n/2)O _{2(g)} → mCO _(g) + (n/2)H _{2(g)}	R6
Carbon-steam reforming	C _(s) + H _{2O(g)} ↔ CO _(g) + H _{2(g)}	R7
Water gas shift	CO _(g) + H _{2O(g)} ↔ CO _{2(g)} + H _{2(g)}	R8
Boudouard reaction	C _(s) + CO _{2(g)} ↔ 2CO _(g)	R9

In the case of the molten carbonate salt mixture (MS), the instant gasification rate approached its maximum value ($8.3 \times 10^{-3} \text{ min}^{-1}$) at ca. 55 °C lower compared to non-catalytic CO₂ gasification experiments. Moreover, the Rco values obtained during MS-assisted gasification were significantly higher, compared to non-catalytic and Ni-assisted catalytic gasification, in the temperature range of 600–800 °C. This remarkable result is in agreement with relevant studies on the MS-assisted CO₂ gasification of various biomass fuels [28,71,81,86,105]. Obviously, MS favors CO production at lower gasification temperatures due to its ability to improve mass and heat transfer phenomena in conjunction with the catalytic role of contained alkali metals in the three-cyclic-step Boudouard reaction (Table 4) [65–67].

Table 4. Mechanism of the alkali carbonate-assisted carbon CO₂ gasification.

Reaction	No
M ₂ CO ₃ + 2C → 2M* + 3CO	R11
2M* + CO ₂ → M ₂ O + CO	R12
M ₂ O + CO ₂ → M ₂ CO ₃	R13
C _(s) + CO _{2(g)} → 2CO _(g)	R14

* M stands for the alkali metal.

Notably, the CO production rate maxima for the combined MS-Ni/X (X: CeO₂, Al₂O₃) medium was shifted to 15, 40, and 70 °C lower compared to MS and Ni catalysts and non-catalytic gasification tests, respectively. Most importantly, the mixed MS-Ni/CeO₂ and MS-Ni/Al₂O₃ composites revealed an excellent synergy regarding their beneficial role in the devolatilization and tar cracking/reforming zones. Indeed, in the temperature range of 300 to 550 °C, the maximum Rco value for both MS-Ni systems was four times higher ($4 \times 10^{-3} \text{ min}^{-1}$, 460 °C) compared to their counterparts. This can be attributed to the combined catalytic effect of both Ni catalysts and MS on tar/volatiles' thermal and/or dry cracking/reforming reactions, as well as on the oxidation of the dissociated carbon on nickel active sites [44,45]. Interestingly, the additional CO formation at this temperature regime coincides with the melting point of the MS (Li₂CO₃-K₂CO₃) which is ca. 490 °C [65]. As the salt mixture melts, it forms a thin layer that favors the carbon-MS contact [68,70]. This in turn facilitates the tar oxidation reaction (R6) at the carbon-catalyst interface through the labile oxygen species in the low temperature region (see H₂-TPR analysis above).

To further shed light on the CO₂ gasification performance, the carbon to CO conversion efficiency, X_{co} (Figure 6), was calculated via Equation 1. Notably, there are three distinct temperature regimes. At temperatures up to 600 °C, where tar and volatiles' cracking/reforming reactions prevail, the combined MS-Ni systems lead to a carbon to CO conversion of ca. 0.3, in complete contrast to the bare constituents (Ni catalysts or MS), which are almost inactive. This further verifies the synergy between the Ni-based catalysts and MS towards tar and volatile dry cracking/reforming reactions. At the temperature range between 600 and 800 °C, the CO production is mainly ascribed to the endothermic Boudouard reaction (R9). In this temperature regime, the X_{co} values for the MS-Ni systems are higher compared to their individual counterparts, highlighting the syner-

getic combination of the MS-induced mass/heat transfer phenomena and catalytic activity towards the Boudouard reaction (R9), along with the Ni ability to favor the C-C bond cleavage reaction into an additional CO formation. At 800 °C, the X_{CO} follows the order: MS-Ni/Ce \approx MS-Ni/Al (0.75) > MS (0.68) > Ni/Ce (0.51) > Ni/Al \approx no catalyst (ca. 0.45). At temperatures higher than 800 °C, the carbon to CO conversion for the combined MS-Ni samples reached a plateau ($X_{CO} = 0.78$) due to fuel depletion above this temperature. The X_{CO} for the MS-assisted gasification tests reached the highest value (0.81 at 950 °C), highlighting the pronounced effect of MS at higher temperatures.

To further explore the synergetic role between NiO and CeO₂ in combination with molten carbonate salt (MS) in the low/intermediate tar cracking/reforming temperature regime, the effect of MS-NiO and MS-CeO₂ systems on the CO₂ gasification reaction rate and carbon to CO conversion was examined (Figure 7). It is evident that the presence of all the catalyst's components is necessary to achieve high gasification performance at temperatures below 700 °C. This coincides with the well-established hydrocarbon (tar) dissociation and dehydrogenation on Ni active sites, the enhanced CeO₂ redox properties in the low/intermediate temperature regime, and the key role of MS on the decomposition of volatiles during steam and/or dry reforming reactions [44,45].

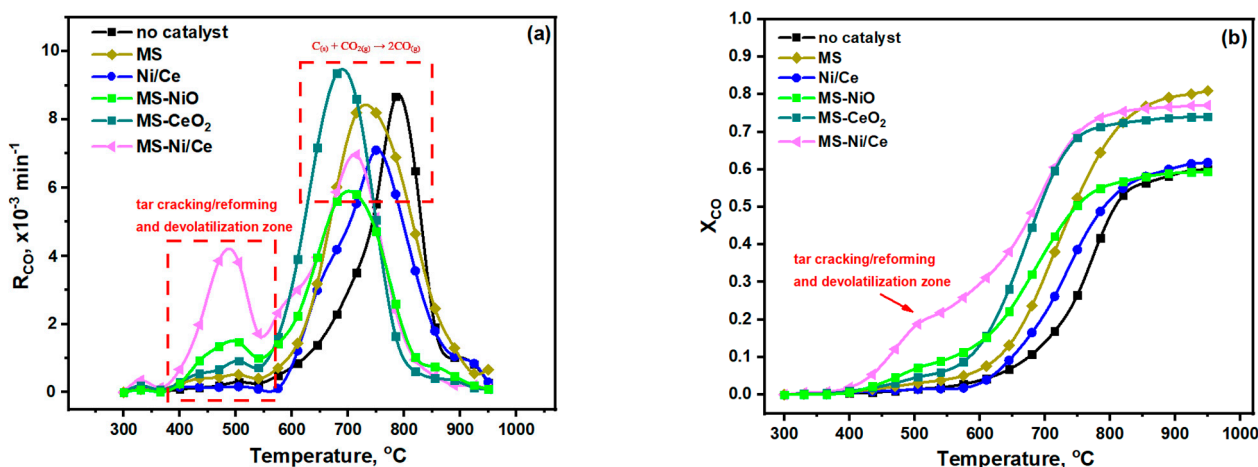


Figure 7. Effect of temperature and catalyst components on the instant CO production rate, R_{CO} (a), and carbon to CO conversion (b) during non-isothermal CO₂ gasification experiments. Gasifying agent flowrate = 30 cm³/min of 20 vol.% CO₂ in Helium.

3. Materials and Methods

3.1. Fuel Feedstock

Olive kernel (OK) from Cretan olive tree cultures was selected as raw fuel. OK was initially crushed to a particle size between 1–3 mm using a jaw crusher. Then, part of this fraction was milled to 100–200 μ m using an agate mortar (Retsch RM200) producing a large amount (ca. 70 wt.%) of fines (<100 μ m). The elemental and proximate analysis of olive kernel fuel has been presented in our previous work [31], following a typical pattern for lignocellulosic residual biomass with negligible nitrogen, sulfur, and chlorine contents. Moreover, the proximate analysis revealed the high volatile matter content (75.8 wt.%) and low ash concentration (2.9 wt.%) of olive kernel biomass.

3.2. Catalyst Preparation

Ni-based catalysts were prepared using the wet impregnation method. Commercial aluminum oxide (α -Al₂O₃, ~100 mesh, 99.9% purity, Aldrich) and cerium oxide (CeO₂, 99.9% purity) were used as catalyst supports. In brief, Ni/Al₂O₃ and Ni/CeO₂ catalysts were prepared by the aqueous impregnation of nickel nitrate precursor salt (Ni(NO₃)₂·6H₂O) in commercial α -Al₂O₃ and CeO₂ by vigorously agitating at ca. 80 °C for about 3 h until a green slurry was obtained. The slurry was dried at 90 °C for 12 h and

then calcined in an air flow at 850 °C for 4 h. The nominal loading of Ni over Al₂O₃ and CeO₂ was set at 15 wt.% based on relevant literature studies and reviews [33,39]. For sake of brevity, the Ni-based catalysts will be noted as Ni/Ce and Ni/Al, with the procedure followed to synthesize the former sample being illustrated in Figure 8.

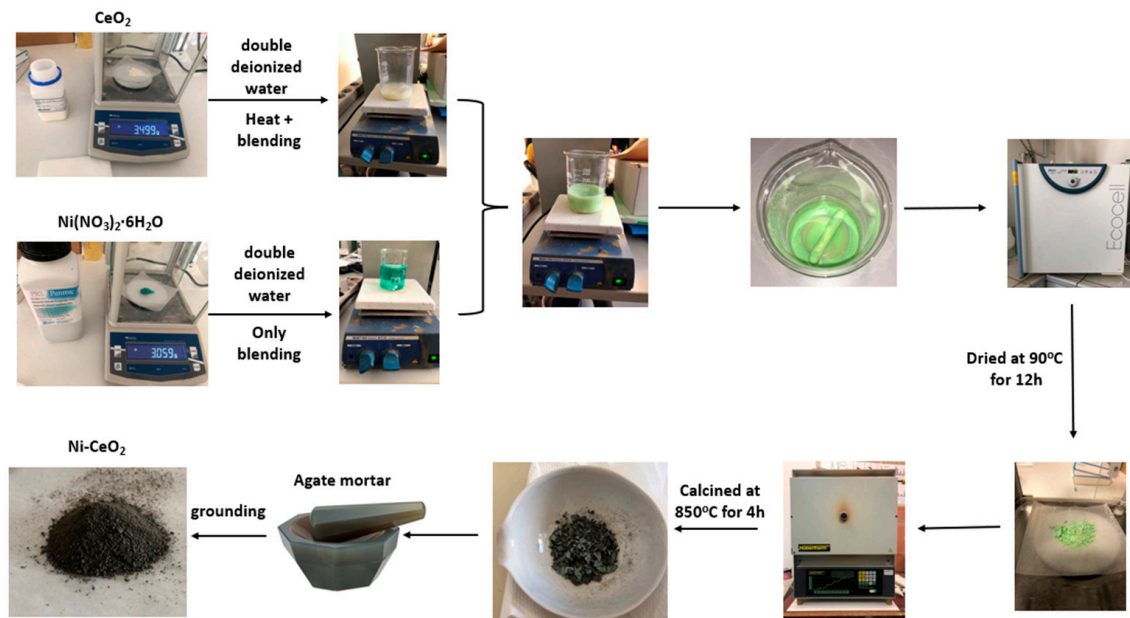


Figure 8. Illustrated procedure for the synthesis of the 15 wt.% Ni/CeO₂ sample.

The molten salts used for preparing the eutectic carbonates mixture were Li₂CO₃ and K₂CO₃ (Sigma Aldrich, Munich, Germany) with a molar ratio of 62/38 mol.%, respectively. The salts were firstly rolled and milled at ca. 200 rpm for approximately 12 h. The melting point of the binary carbonates eutectic mixture (MS) is approximately 498 °C, thus it could be utilized as a mass and heat transfer medium for the gasification of solid fuels [65]. Then the Li₂-K₂/CO₃ mixture (MS) was placed on a hot plate at 60 °C so as to evaporate the liquid carrier (ethanol) used during the roll milling process [65]. Finally, the molten salts were cooled to room temperature, crushed, and finely ground in an agate mortar.

The combined Ni/M_xO_y (M: Al, Ce) and MS blends were prepared by homogeneously mixing the individual counterparts in an agate mortar.

3.3. Experimental Apparatus for the Olive Kernel Catalytic Gasification Studies

Figure 9 schematically illustrates the experimental setup for the olive kernel catalytic gasification tests, which were performed under a batch mode of operation. The experimental apparatus and conditions are described in detail in our previous work [31]. In brief, a mixture of fuel feedstock (0.1 g) and MS or MS-Ni catalyst was loaded into an Inox, U-tube, fixed bed reactor. The employed catalyst-to-biomass weight ratio was fixed at 0.5:1 for the MS-OK experiments, 2.5:1 for the Ni-aided gasification tests, and 0.5:2:1 for the ternary MS-Ni catalyst/OK mixtures. The mass ratio of the employed catalysts to OK was fixed at 2.5, while the MS to OK weight ratio was set at 0.5. The feedstock mixtures were prepared by physically mixing the olive kernel with the examined catalyst composites in an agate mortar. The flowrate of 20 vol.% CO₂/He, used as gasifying agent mixture, was set at 30 cm³/min. After passing through a cooling trap (ice bath) to collect tars, the gaseous products were driven to a gas chromatograph (Shimadzu GC-14B) to monitor the effluent's gas composition in the temperature range of 300–950 °C, by increasing the temperature at a constant rate of 2 °C/min. In order to obtain reliable and accurate results, all gasification tests were repeated at least twice.

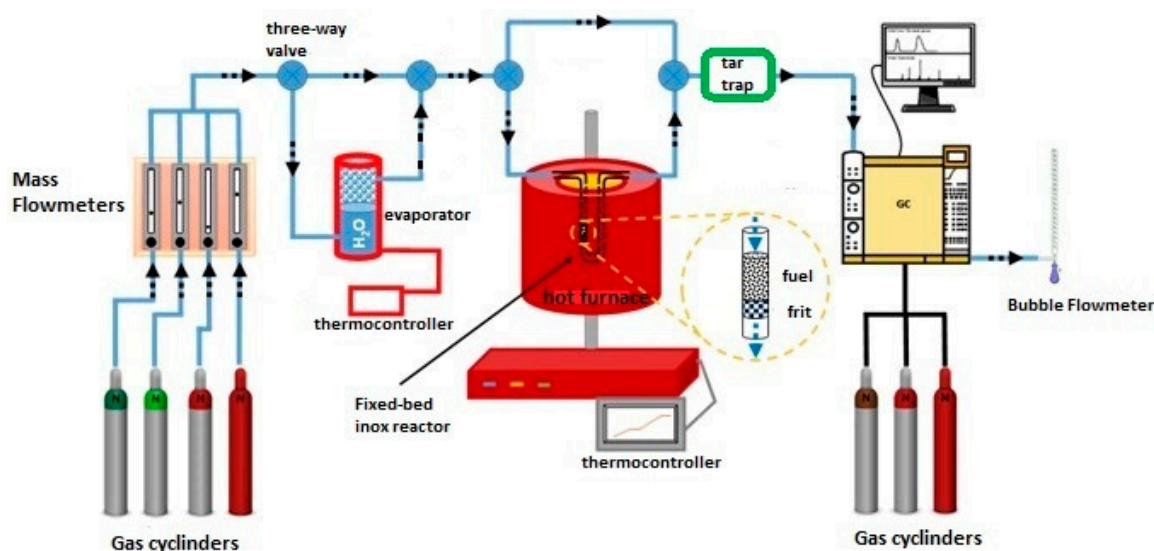


Figure 9. Experimental apparatus of the lab-scale CO₂-gasification experiments.

Here, it should be noted that non-isothermal gasification studies provide a more reliable overview on the gasification performance in the whole operational range since the gasification temperature often varies along the gasifier in real applications. Moreover, lower heating rates result in more accurate studies since higher ones may lead to the formation of larger temperature gradients within the sample, leading to higher temperature differences inside the fuel bed [106].

3.4. Gasification Performance Indicators

In the case of the non-isothermal catalytic CO₂-gasification experiments, since CO was practically the main product during gasification, the catalysts' activity was evaluated through the calculation of two performance parameters: X_{CO} expressing the carbon to CO conversion; and R_{CO} (min⁻¹) standing for the instant CO production rate, as described in our previous work [107]:

$$X_{CO} = \frac{\sum_{t=0}^{t_{step1}} y_{CO,t} \times 12}{m \times w_c} + \frac{\sum_{t_{step1}}^{t_f} y_{CO,t} \times 12}{2 \times m \times w_c} \quad (1)$$

$$R_{CO} = \frac{dX_{CO}}{dt} \quad (2)$$

where $y_{CO,t}$ corresponds to the cumulative CO production moles in time t , m is the initial mass of fuel sample (gr), and w_c is the elemental carbon content of the olive kernel biomass fuel. It should be noted that the first term in Equation (1) stands for the CO production during the devolatilization stage, whereas the second term corresponds to the CO formation associated with the Boudouard reaction ($C + CO_2 \rightarrow 2 CO$) during the gasification stage. The same expression has also been employed in relevant studies in the literature to estimate the CO₂ gasification conversion of various coal fuels [81,101].

3.5. Physicochemical Characterizations

X-ray diffraction patterns of powdered samples were obtained by a Bruker AXS D8 Advance copper anode diffractometer (CuK α radiation) equipped with a nickel foil monochromator, operating at 40 kV and 40 mA over the 2θ collection range of 10–80° at a scan rate of 0.05° s⁻¹.

The d-spacing was calculated by applying the Bragg's law:

$$2d \sin\theta_B = n \lambda \quad (3)$$

where λ is the X-ray wavelength, d is the spacing of the diffraction planes, and θ_B is the angle between the incident rays and the diffracting planes, otherwise known as the Bragg angle. For CeO_2 and NiO , which are both crystallized in cubic form ($a = b = c$, $\alpha = \beta = \gamma = 90^\circ$), the lattice parameters can be calculated by the following equation:

$$1/d^2 = (h^2 + k^2 + l^2)/a^2 \quad (4)$$

The morphological analysis of the samples was performed by scanning electron microscopy (SEM, JEOL JSM-6390LV, JEOL Ltd., Akishima, Tokyo, Japan) operating at 20 keV. Elemental analysis/mapping and morphological observation were obtained by high-resolution scanning electron microscopy (HR-SEM) using a JS-IT700HR (JEOL, Tokyo, Japan) instrument at 20 kV. Transmission electron microscopy (TEM) was performed using a JEM-2100 instrument (JEOL, Tokyo, Japan) equipped with a LaB6 filament, working at 200 kV. Specimens for TEM were prepared by the deposition of dispersed powder samples after ultrasonication.

The reducibility of the Ni/Ce and Ni/Al catalysts was examined by temperature-programmed reduction with H_2 (TPR- H_2). In a typical experiment, 0.1 g of the catalyst sample was loaded in a fixed-bed quartz reactor and pretreated at 500 °C for one hour under helium flow (50 mL/min). The catalyst was then cooled down to 35–40 °C, and TPR- H_2 analysis was carried out from 40 to 920 °C at a heating rate of 10 °C/min in a 5 v/v% H_2/He flow (50 mL/min). The composition of the exit gas was monitored online with a quadrupole mass analyzer (Omnistar, Balzer). The m/z fragments registered were as follows: $\text{H}_2 = 2$, $\text{H}_2\text{O} = 18$, and $\text{He} = 4$. The quantitative analysis of the consumed/desorbed H_2 was based on $m/z = 2$.

4. Conclusions

The main objective of this work was to explore the impact of catalyst addition (Ni/ CeO_2 , Ni/ Al_2O_3) and/or carbonates (eutectic binary mixture of carbonate salts, MS) on the CO_2 gasification of olive kernel biomass fuel. It was found that Ni/ CeO_2 and Ni/ Al_2O_3 catalysts demonstrated a beneficial role on CO_2 gasification performance by slightly reducing the onset and peak CO_2 gasification temperatures. Interestingly, the Ni/ CeO_2 catalyst presented an enhanced instant gasification reaction rate for temperatures up to 800 °C, in line with the significant redox capability of CeO_2 . In the presence of MS, the instant gasification rate approached its maximum value ($8.3 \times 10^{-3} \text{ min}^{-1}$) at ca. 55 °C lower compared to the non-catalytic gasification tests. The pronounced effect of MS at higher temperatures was also reflected in the high carbon to CO conversion value ($X_{\text{CO}} = 0.81$ at 950 °C). More importantly, the combined use of MS with Ni catalysts notably enhances the CO_2 gasification performance, specifically on the devolatilization and tar cracking/reforming zones. Indeed, in the temperature range of 300 to 550 °C, the maximum R_{CO} and X_{CO} values for both MS-Ni systems were notably higher ($4 \times 10^{-3} \text{ min}^{-1}$ and 0.25 at 460 °C) compared to the insignificant corresponding performance ($R_{\text{CO}} < 0.5 \times 10^{-3} \text{ min}^{-1}$) obtained by the individual catalyst counterparts. Collectively, the synergistic combination of molten salt and nickel-based catalysts can provide an innovative approach to enhance biomass CO_2 gasification and, in parallel, improve syngas quality for downstream processes, substantially reducing syngas cleaning requirements and system costs.

Author Contributions: A.L., V.B., L.Z., S.S. (Sofia Stefa), S.A.K. and G.V. contributed to samples preparation and characterization; A.L. and S.S. (Stavros Spyridakos) contributed to gasification studies; A.L., G.E.M. and M.K. contributed to the conception, design, and results interpretation; G.E.M. and M.K. validated the results and administered the project. A.L. wrote the original draft. Finally, A.L., G.E.M. and M.K. reviewed, edited, and submitted the manuscript in the final form. All authors have read and agreed to the published version of the manuscript.

Funding: This research has been co-financed by the project “Development of New Innovative Low Carbon Footprint Energy Technologies to Enhance Excellence in the Region of Western Macedonia”(MIS 5047197), which is implemented under the action “Reinforcement of the Research and Innovation Infrastructure”, funded by the Operational Programme “Competitiveness, Entrepreneurship and Innovation” (NSRF 2014–2020) and co-financed by Greece and the European Union (European Regional Development Fund).

Conflicts of Interest: The authors declare no conflict of interest.

References

1. Brown, R.C. The Role of Pyrolysis and Gasification in a Carbon Negative Economy. *Processes* **2021**, *9*, 882. [CrossRef]
2. Varvoutis, G.; Lampropoulos, A.; Mandela, E.; Konsolakis, M. Recent Advances on CO₂ Mitigation Technologies: On the Role of Hydrogenation Route via Green H₂. *Energies* **2022**, *15*, 4790. [CrossRef]
3. Zhang, X. Essential Scientific Mapping of the Value Chain of Thermochemically Converted Second-Generation Bio-Fuels. *Green Chem.* **2016**, *18*, 5086–5117. [CrossRef]
4. Mishra, S.; Upadhyay, R.K. Review on Biomass Gasification: Gasifiers, Gasifying Mediums, and Operational Parameters. *Mater. Sci. Energy Technol.* **2021**, *4*, 329–340. [CrossRef]
5. Di Giuliano, A.; Funcia, I.; Pérez-Vega, R.; Gil, J.; Gallucci, K. Novel Application of Pretreatment and Diagnostic Method Using Dynamic Pressure Fluctuations to Resolve and Detect Issues Related to Biogenic Residue Ash in Chemical Looping Gasification. *Processes* **2020**, *8*, 1137. [CrossRef]
6. Narnaware, S.L.; Panwar, N.L. Biomass Gasification for Climate Change Mitigation and Policy Framework in India: A Review. *Bioresour. Technol. Reports* **2022**, *17*, 100892. [CrossRef]
7. Allesina, G.; Pedrazzi, S. Barriers to Success: A Technical Review on the Limits and Possible Future Roles of Small Scale Gasifiers. *Energies* **2021**, *14*, 6711. [CrossRef]
8. Ongen, A.; Ozgu, C.; Ayol, A. ScienceDirect Biomass Gasification for Sustainable Energy Production: A Review. *Int. J. Hydrog. Energy* **2022**, *47*, 15419–15433. [CrossRef]
9. Pio, D.T.; Tarelho, L.A.C. Industrial Gasification Systems (>3 MWth) for Bioenergy in Europe: Current Status and Future Perspectives. *Renew. Sustain. Energy Rev.* **2021**, *145*, 111108. [CrossRef]
10. Situmorang, Y.A.; Zhao, Z.; Yoshida, A.; Abudula, A.; Guan, G. Small-Scale Biomass Gasification Systems for Power Generation (<200 kW Class): A Review. *Renew. Sustain. Energy Rev.* **2020**, *117*, 109486. [CrossRef]
11. Aravani, V.P.; Sun, H.; Yang, Z.; Liu, G.; Wang, W.; Anagnostopoulos, G.; Syriopoulos, G.; Charisiou, N.D.; Goula, M.A.; Kornaros, M.; et al. Agricultural and Livestock Sector’s Residues in Greece & China: Comparative Qualitative and Quantitative Characterization for Assessing Their Potential for Biogas Production. *Renew. Sustain. Energy Rev.* **2022**, *154*, 111821. [CrossRef]
12. Marks, E.A.N.; Kinigopoulou, V.; Akrou, H.; Azzaz, A.A.; Doulgeris, C.; Jellali, S.; Rad, C.; Zulueta, P.S.; Tziritis, E.; El-Bassi, L.; et al. Potential for Production of Biochar-Based Fertilizers from Olive Millwaste in Mediterranean Basin Countries: An Initial Assessment for Spain, Tunisia, and Greece. *Sustainability* **2020**, *12*, 6081. [CrossRef]
13. Diez, C.M.; Trujillo, I.; Martínez-Urdiroz, N.; Barranco, D.; Rallo, L.; Marfil, P.; Gaut, B.S. Olive Domestication and Diversification in the Mediterranean Basin. *New Phytol.* **2015**, *206*, 436–447. [CrossRef]
14. del Mar Contreras, M.; Romero, I.; Moya, M.; Castro, E. Olive-Derived Biomass as a Renewable Source of Value-Added Products. *Process Biochem.* **2020**, *97*, 43–56. [CrossRef]
15. García Martín, J.F.; Cuevas, M.; Feng, C.; Mateos, P.Á.; Torres, M. Energetic Valorisation of Olive Biomass: Olive-Tree Pruning, Olive Stones and Pomaces. *Processes* **2020**, *8*, 511. [CrossRef]
16. Christoforou, E.; Fokaides, P.A. A Review of Olive Mill Solid Wastes to Energy Utilization Techniques. *Waste Manag.* **2016**, *49*, 346–363. [CrossRef]
17. Damartzis, T.; Michailos, S.; Zabaniotou, A. Energetic Assessment of a Combined Heat and Power Integrated Biomass Gasification-Internal Combustion Engine System by Using Aspen Plus[®]. *Fuel Process. Technol.* **2012**, *95*, 37–44. [CrossRef]
18. Vera, D.; Jurado, F.; Margaritis, N.K.; Grammelis, P. Experimental and Economic Study of a Gasification Plant Fuelled with Olive Industry Wastes. *Energy Sustain. Dev.* **2014**, *23*, 247–257. [CrossRef]
19. Vera, D.; De Mena, B.; Jurado, F.; Schories, G. Study of a Downdraft Gasifier and Gas Engine Fueled with Olive Oil Industry Wastes. *Appl. Therm. Eng.* **2013**, *51*, 119–129. [CrossRef]
20. Fryda, L.; Panopoulos, K.D.; Kakaras, E. Integrated CHP with Autothermal Biomass Gasification and SOFC-MGT. *Energy Convers. Manag.* **2008**, *49*, 281–290. [CrossRef]
21. Manara, P.; Zabaniotou, A. Indicator-Based Economic, Environmental, and Social Sustainability Assessment of a Small Gasification Bioenergy System Fuelled with Food Processing Residues from the Mediterranean Agro-Industrial Sector. *Sustain. Energy Technol. Assessments* **2014**, *8*, 159–171. [CrossRef]
22. Vera, D.; Jurado, F.; De Mena, B.; Hernández, J.C. A Distributed Generation Hybrid System for Electric Energy Boosting Fueled with Olive Industry Wastes. *Energies* **2019**, *12*, 500. [CrossRef]

23. Kougioumtzis, M.A.; Kanaveli, I.P.; Karampinis, E.; Grammelis, P.; Kakaras, E. Combustion of Olive Tree Pruning Pellets versus Sunflower Husk Pellets at Industrial Boiler. Monitoring of Emissions and Combustion Efficiency. *Renew. Energy* **2021**, *171*, 516–525. [[CrossRef](#)]
24. Colantoni, A.; Villarini, M.; Marcantonio, V.; Gallucci, F.; Cecchini, M. Performance Analysis of a Small-Scale ORC Trigeneration System Powered by the Combustion of Olive Pomace. *Energies* **2019**, *12*, 2279. [[CrossRef](#)]
25. Alatzas, S.; Moustakas, K.; Malamis, D.; Vakalis, S. Biomass Potential from Agricultural Waste for Energetic Utilization in Greece. *Energies* **2019**, *12*, 1095. [[CrossRef](#)]
26. Vourdoubas, J. Use of Renewable Energy Sources for Energy Generation in Rural Areas in the Island of Crete, Greece. *Eur. J. Environ. Earth Sci.* **2020**, *1*, 1–7. [[CrossRef](#)]
27. Vourdoubas, J. Description and Assessment of a Small Renewable Energy Community in the Island of Crete, Greece. *Open J. Energy Effic.* **2017**, *06*, 97–111. [[CrossRef](#)]
28. Ratchahat, S.; Kodama, S.; Tanthapanichakoon, W.; Sekiguchi, H. CO₂ Gasification of Biomass Wastes Enhanced by Ni/Al₂O₃ Catalyst in Molten Eutectic Carbonate Salt. *Int. J. Hydrogen Energy* **2015**, *40*, 11809–11822. [[CrossRef](#)]
29. Teh, J.S.; Teoh, Y.H.; How, H.G.; Sher, F. Thermal Analysis Technologies for Biomass Feedstocks: A State-of-the-Art Review. *Processes* **2021**, *9*, 1610. [[CrossRef](#)]
30. Suárez-Ruiz, I.; Diez, M.A.; Rubiera, F. *New Trends in Coal Conversion: Combustion, Gasification, Emissions, and Coking*; Elsevier: Amsterdam, The Netherlands, 2018; ISBN 9780081022016.
31. Lampropoulos, A.; Kaklidis, N.; Athanasiou, C.; Montes-Morán, M.A.; Arenillas, A.; Menéndez, J.A.; Binas, V.D.; Konsolakis, M.; Marnellos, G.E. Effect of Olive Kernel Thermal Treatment (Torrefaction vs. Slow Pyrolysis) on the Physicochemical Characteristics and the CO₂ or H₂O Gasification Performance of as-Prepared Biochars. *Int. J. Hydrogen Energy* **2020**, *46*, 29126–29141. [[CrossRef](#)]
32. Lampropoulos, A.; Binas, V.; Konsolakis, M.; Marnellos, G.E. Steam Gasification of Greek Lignite and Its Chars by Co-Feeding CO₂ toward Syngas Production with an Adjustable H₂/CO Ratio. *Int. J. Hydrogen Energy* **2021**, *46*, 28486–28500. [[CrossRef](#)]
33. Galadima, A.; Masudi, A.; Muraza, O. Catalyst Development for Tar Reduction in Biomass Gasification: Recent Progress and the Way Forward. *J. Environ. Manage.* **2022**, *305*, 114274. [[CrossRef](#)] [[PubMed](#)]
34. Lee, D.; Nam, H.; Won Seo, M.; Hoon Lee, S.; Tokmurzin, D.; Wang, S.; Park, Y.K. Recent Progress in the Catalytic Thermochemical Conversion Process of Biomass for Biofuels. *Chem. Eng. J.* **2022**, *447*, 137501. [[CrossRef](#)]
35. Straczewski, G.; Mai, R.; Gerhards, U.; Garbev, K.; Leibold, H. Catalytic Tar Conversion in Two Different Hot Syngas Cleaning Systems. *Catalysts* **2021**, *11*, 1231. [[CrossRef](#)]
36. Guan, G.; Kaewpanha, M.; Hao, X.; Abudula, A. Catalytic Steam Reforming of Biomass Tar: Prospects and Challenges. *Renew. Sustain. Energy Rev.* **2016**, *58*, 450–461. [[CrossRef](#)]
37. Mun, T.Y.; Seon, P.G.; Kim, J.S. Production of a Producer Gas from Woody Waste via Air Gasification Using Activated Carbon and a Two-Stage Gasifier and Characterization of Tar. *Fuel* **2010**, *89*, 3226–3234. [[CrossRef](#)]
38. Guo, F.; Jia, X.; Liang, S.; Zhou, N.; Chen, P.; Ruan, R. Development of Biochar-Based Nanocatalysts for Tar Cracking/Reforming during Biomass Pyrolysis and Gasification. *Bioresour. Technol.* **2020**, *298*, 122263. [[CrossRef](#)]
39. Ren, J.; Cao, J.P.; Zhao, X.Y.; Yang, F.L.; Wei, X.Y. Recent Advances in Syngas Production from Biomass Catalytic Gasification: A Critical Review on Reactors, Catalysts, Catalytic Mechanisms and Mathematical Models. *Renew. Sustain. Energy Rev.* **2019**, *116*, 109426. [[CrossRef](#)]
40. Binte Mohamed, D.K.; Veksha, A.; Ha, Q.L.M.; Chan, W.P.; Lim, T.T.; Lisak, G. Advanced Ni Tar Reforming Catalysts Resistant to Syngas Impurities: Current Knowledge, Research Gaps and Future Prospects. *Fuel* **2022**, *318*, 123602. [[CrossRef](#)]
41. Ren, J.; Cao, J.P.; Zhao, X.Y.; Liu, Y.L. Recent Progress and Perspectives of Catalyst Design and Downstream Integration in Biomass Tar Reforming. *Chem. Eng. J.* **2022**, *429*, 132316. [[CrossRef](#)]
42. Wu, Y.; Wang, H.; Li, H.; Han, X.; Zhang, M.; Sun, Y.; Fan, X.; Tu, R.; Zeng, Y.; Xu, C.C.; et al. Applications of Catalysts in Thermochemical Conversion of Biomass (Pyrolysis, Hydrothermal Liquefaction and Gasification): A Critical Review. *Renew. Energy* **2022**, *196*, 462–481. [[CrossRef](#)]
43. Qin, T.; Yuan, S. Research Progress of Catalysts for Catalytic Steam Reforming of High Temperature Tar: A Review. *Fuel* **2023**, *331*, 125790. [[CrossRef](#)]
44. Gao, N.; Salisu, J.; Quan, C.; Williams, P. Modified Nickel-Based Catalysts for Improved Steam Reforming of Biomass Tar: A Critical Review. *Renew. Sustain. Energy Rev.* **2021**, *145*, 111023. [[CrossRef](#)]
45. Chan, F.L.; Tanksale, A. Review of Recent Developments in Ni-Based Catalysts for Biomass Gasification. *Renew. Sustain. Energy Rev.* **2014**, *38*, 428–438. [[CrossRef](#)]
46. Abedi, A.; Dalai, A.K. Steam Gasification of Oat Hull Pellets over Ni-Based Catalysts: Syngas Yield and Tar Reduction. *Fuel* **2019**, *254*, 115585. [[CrossRef](#)]
47. Hu, J.; Jia, Z.; Zhao, S.; Wang, W.; Zhang, Q.; Liu, R.; Huang, Z. Activated Char Supported Fe-Ni Catalyst for Syngas Production from Catalytic Gasification of Pine Wood. *Bioresour. Technol.* **2021**, *340*, 125600. [[CrossRef](#)]
48. Khalifa, O.; Xu, M.; Zhang, R.; Iqbal, T.; Li, M.; Lu, Q. Steam Reforming of Toluene as a Tar Model Compound with Modified Nickel-Based Catalyst. *Front. Energy* **2021**, *16*, 492–501. [[CrossRef](#)]
49. Lu, Y.; Jin, H.; Zhang, R. Evaluation of Stability and Catalytic Activity of Ni Catalysts for Hydrogen Production by Biomass Gasification in Supercritical Water. *Carbon Resour. Convers.* **2019**, *2*, 95–101. [[CrossRef](#)]

50. Granados-Fernández, R.; Cortés-Reyes, M.; Poggio-Fraccari, E.; Herrera, C.; Larrubia, M.; Alemany, L.J. Biomass Catalytic Gasification Performance over Unsupported Ni-Ce Catalyst for High-Yield Hydrogen Production. *Biofuels Bioprod. Biorefining* **2020**, *14*, 20–29. [[CrossRef](#)]
51. Baker, E.G.; Mudge, L.K.; Brown, M.D. Steam Gasification of Biomass with Nickel Secondary Catalysts. *Ind. Eng. Chem. Res.* **1987**, *26*, 1335–1339. [[CrossRef](#)]
52. Li, X.T.; Grace, J.R.; Lim, C.J.; Watkinson, A.P.; Chen, H.P.; Kim, J.R. Biomass Gasification in a Circulating Fluidized Bed. *Biomass Bioenergy* **2004**, *26*, 171–193. [[CrossRef](#)]
53. Ashok, J.; Kawi, S. Steam Reforming of Toluene as a Biomass Tar Model Compound over CeO₂ Promoted Ni/CaOeAl₂O₃ Catalytic Systems. *Int. J. Hydrogen Energy* **2013**, *38*, 13938–13949. [[CrossRef](#)]
54. Furusawa, T.; Saito, K.; Kori, Y.; Miura, Y.; Sato, M.; Suzuki, N. Steam Reforming of Naphthalene/Benzene with Various Types of Pt- and Ni-Based Catalysts for Hydrogen Production. *Fuel* **2013**, *103*, 111–121. [[CrossRef](#)]
55. Artetxe, M.; Nahil, M.A.; Olazar, M.; Williams, P.T. Steam Reforming of Phenol as Biomass Tar Model Compound over Ni/Al₂O₃ Catalyst. *Fuel* **2016**, *184*, 629–636. [[CrossRef](#)]
56. Artetxe, M.; Alvarez, J.; Nahil, M.A.; Olazar, M.; Williams, P.T. Steam Reforming of Different Biomass Tar Model Compounds over Ni/Al₂O₃ Catalysts. *Energy Convers. Manag.* **2017**, *136*, 119–126. [[CrossRef](#)]
57. Kihlman, J.; Simell, P. Carbon Formation in the Reforming of Simulated Biomass Gasification Gas on Nickel and Rhodium Catalysts. *Catalysts* **2022**, *12*, 410. [[CrossRef](#)]
58. Tomishige, K.; Kimura, T.; Nishikawa, J.; Miyazawa, T.; Kunimori, K. Promoting Effect of the Interaction between Ni and CeO₂ on Steam Gasification of Biomass. *Catal. Commun.* **2007**, *8*, 1074–1079. [[CrossRef](#)]
59. Park, H.J.; Park, S.H.; Sohn, J.M.; Park, J.; Jeon, J.K.; Kim, S.S.; Park, Y.K. Steam Reforming of Biomass Gasification Tar Using Benzene as a Model Compound over Various Ni Supported Metal Oxide Catalysts. *Bioresour. Technol.* **2010**, *101*, S101–S103. [[CrossRef](#)] [[PubMed](#)]
60. Abou Rached, J.; El Hayek, C.; Dahdah, E.; Gennequin, C.; Aouad, S.; Tidahy, H.L.; Estephane, J.; Nsouli, B.; Aboukaïs, A.; Abi-Aad, E. Ni Based Catalysts Promoted with Cerium Used in the Steam Reforming of Toluene for Hydrogen Production. *Int. J. Hydrogen Energy* **2017**, *42*, 12829–12840. [[CrossRef](#)]
61. Lu, Y.; Li, S.; Guo, L.; Zhang, X. Hydrogen Production by Biomass Gasification in Supercritical Water over Ni/ γ -Al₂O₃ and Ni/CeO₂- γ -Al₂O₃ Catalysts. *Int. J. Hydrogen Energy* **2010**, *35*, 7161–7168. [[CrossRef](#)]
62. Nishikawa, J.; Nakamura, K.; Asadullah, M.; Miyazawa, T.; Kunimori, K.; Tomishige, K. Catalytic Performance of Ni/CeO₂/Al₂O₃ Modified with Noble Metals in Steam Gasification of Biomass. *Catal. Today* **2008**, *131*, 146–155. [[CrossRef](#)]
63. Łamacz, A. Toluene Steam Reforming over Ni/CeZrO₂—The Influence of Performance and Carbon Deposition. *Catalysts* **2022**, *12*, 219. [[CrossRef](#)]
64. Hernandez, A.R.C.; Castañeda, D.G.G.; Enriquez, A.S.; de Lasa, H.; Rosales, B.S. Ru-Promoted Ni/ γ -Al₂O₃ Fluidized Catalyst for Biomass Gasification. *Catalysts* **2020**, *10*, 316. [[CrossRef](#)]
65. Frangini, S.; Masi, A. Molten Carbonates for Advanced and Sustainable Energy Applications: Part I. Revisiting Molten Carbonate Properties from a Sustainable Viewpoint. *Int. J. Hydrogen Energy* **2016**, *41*, 18739–18746. [[CrossRef](#)]
66. Abdalazeez, A.; Li, T.; Wang, W.; Abuelgasim, S. A Brief Review of CO₂ utilization for Alkali Carbonate Gasification and Biomass/Coal Co-Gasification: Reactivity, Products and Process. *J. CO₂ Util.* **2021**, *43*, 101370. [[CrossRef](#)]
67. Yu, J.; Guo, Q.; Gong, Y.; Ding, L.; Wang, J.; Yu, G. A Review of the Effects of Alkali and Alkaline Earth Metal Species on Biomass Gasification. *Fuel Process. Technol.* **2021**, *214*, 106723. [[CrossRef](#)]
68. Mckee, D.W. Gasification of Graphite in CO₂ and Water Vapor- the Catalytic Effect of Metal Salts. *Carbon N. Y.* **1982**, *20*, 59–66. [[CrossRef](#)]
69. Wen, W.Y. Mechanisms of Alkali Metal Catalysis in the Gasification of Coal, Char, or Graphite. *Catal. Rev.* **1980**, *22*, 1–28. [[CrossRef](#)]
70. Mallick, D.; Mahanta, P.; Moholkar, V.S. Co-Gasification of Coal and Biomass Blends: Chemistry and Engineering. *Fuel* **2017**, *204*, 106–128. [[CrossRef](#)]
71. Jia, S.; Ning, S.; Ying, H.; Sun, Y.; Xu, W.; Yin, H. High Quality Syngas Production from Catalytic Gasification of Woodchip Char. *Energy Convers. Manag.* **2017**, *151*, 457–464. [[CrossRef](#)]
72. Nzihou, A.; Stanmore, B.; Sharrock, P. A Review of Catalysts for the Gasification of Biomass Char, with Some Reference to Coal. *Energy* **2013**, *58*, 305–317. [[CrossRef](#)]
73. Freriks, I.L.C.; van Wechem, H.M.H.; Stuiver, J.C.M.; Bouwman, R. Potassium-Catalysed Gasification of Carbon with Steam: A Temperature-Programmed Desorption and Fourier Transform Infrared Study. *Fuel* **1981**, *60*, 463–470. [[CrossRef](#)]
74. Di Blasi, C. Combustion and Gasification Rates of Lignocellulosic Chars. *Prog. Energy Combust. Sci.* **2009**, *35*, 121–140. [[CrossRef](#)]
75. Olivares, R.I.; Chen, C.; Wright, S. The Thermal Stability of Molten Lithium-Sodium-Potassium Carbonate and the Influence of Additives on the Melting Point. *J. Sol. Energy Eng. Trans. ASME* **2012**, *134*, 041002. [[CrossRef](#)]
76. Ratchahat, S.; Kodama, S.; Tanthapanichakoon, W.; Sekiguchi, H. Combined Molten Salt-Ni/Al₂O₃ as Synergistic Medium for High-Quality Syngas Production. *Chem. Eng. J.* **2015**, *278*, 224–233. [[CrossRef](#)]
77. Parvez, A.M.; Afzal, M.T.; Victor Hebb, T.G.; Schmid, M. Utilization of CO₂ in Thermochemical Conversion of Biomass for Enhanced Product Properties: A Review. *J. CO₂ Util.* **2020**, *40*, 101217. [[CrossRef](#)]

78. Lahijani, P.; Zainal, Z.A.; Mohammadi, M.; Mohamed, A.R. Conversion of the Greenhouse Gas CO₂ to the Fuel Gas CO via the Boudouard Reaction: A Review. *Renew. Sustain. Energy Rev.* **2015**, *41*, 615–632. [[CrossRef](#)]
79. Roncancio, R.; Gore, J.P. CO₂ Char Gasification: A Systematic Review from 2014 to 2020. *Energy Convers. Manag.* **2021**, *10*, 100060. [[CrossRef](#)]
80. Renganathan, T.; Yadav, M.V.; Pushpavanam, S.; Voolapalli, R.K.; Cho, Y.S. CO₂ Utilization for Gasification of Carbonaceous Feedstocks: A Thermodynamic Analysis. *Chem. Eng. Sci.* **2012**, *83*, 159–170. [[CrossRef](#)]
81. Xie, Y.; Yang, H.; Zeng, K.; Zhu, Y.; Hu, J.; Mao, Q.; Liu, Q.; Chen, H. Study on CO₂ Gasification of Biochar in Molten Salts: Reactivity and Structure Evolution. *Fuel* **2019**, *254*, 115614. [[CrossRef](#)]
82. Iwaki, H.; Ye, S.; Katagiri, H.; Kitagawa, K. Wastepaper Gasification with CO₂ or Steam Using Catalysts of Molten Carbonates. *Appl. Catal. A Gen.* **2004**, *270*, 237–243. [[CrossRef](#)]
83. Kirtania, K.; Axelsson, J.; Matsakas, L.; Christakopoulos, P.; Umeki, K.; Furujsjö, E. Kinetic Study of Catalytic Gasification of Wood Char Impregnated with Different Alkali Salts. *Energy* **2017**, *118*, 1055–1065. [[CrossRef](#)]
84. Jin, G.; Iwaki, H.; Arai, N.; Kitagawa, K. Study on the Gasification of Wastepaper/Carbon Dioxide Catalyzed by Molten Carbonate Salts. *Energy* **2005**, *30*, 1192–1203. [[CrossRef](#)]
85. Sadhwani, N.; Adhikari, S.; Eden, M.R.; Wang, Z.; Baker, R. Southern Pines Char Gasification with CO₂—Kinetics and Effect of Alkali and Alkaline Earth Metals. *Fuel Process. Technol.* **2016**, *150*, 64–70. [[CrossRef](#)]
86. Kramb, J.; Gómez-Barea, A.; DeMartini, N.; Romar, H.; Doddapaneni, T.R.K.C.; Konttinen, J. The Effects of Calcium and Potassium on CO₂ Gasification of Birch Wood in a Fluidized Bed. *Fuel* **2017**, *196*, 398–407. [[CrossRef](#)]
87. Vamvuka, D.; Karouki, E.; Sfakiotakis, S.; Salatino, P. Gasification of Waste Biomass Chars by Carbon Dioxide via Thermogravimetry-Effect of Catalysts. *Combust. Sci. Technol.* **2012**, *184*, 64–77. [[CrossRef](#)]
88. Song, Q.; Wang, X.; Gu, C.; Wang, N.; Li, H.; Su, H.; Huo, J.; Qiao, Y. A Comprehensive Model of Biomass Char-CO₂ Gasification Reactivity with Inorganic Element Catalysis in the Kinetic Control Zone Based on TGA Analysis. *Chem. Eng. J.* **2020**, *398*, 125624. [[CrossRef](#)]
89. Fatimah, S.; Ragadhita, R.; Al Husaeni, D.F.; Nandiyanto, A.B.D. How to Calculate Crystallite Size from X-Ray Diffraction (XRD) Using Scherrer Method. *ASEAN J. Sci. Eng.* **2021**, *2*, 65–76. [[CrossRef](#)]
90. Bampenrat, A.; Meeyoo, V.; Kitiyanan, B.; Rangsunvigit, P.; Rirksomboon, T. Naphthalene Steam Reforming over Mn-Doped CeO₂-ZrO₂ Supported Nickel Catalysts. *Appl. Catal. A Gen.* **2010**, *373*, 154–159. [[CrossRef](#)]
91. Lee, Y.H.; Ahn, J.Y.; Nguyen, D.D.; Chang, S.W.; Kim, S.S.; Lee, S.M. Role of Oxide Support in Ni Based Catalysts for CO₂ Methanation. *RSC Adv.* **2021**, *11*, 17648–17657. [[CrossRef](#)]
92. Ding, M.Y.; Tu, J.Y.; Wang, T.J.; Ma, L.L.; Wang, C.G.; Chen, L.G. Bio-Syngas Methanation towards Synthetic Natural Gas (SNG) over Highly Active Al₂O₃-CeO₂ Supported Ni Catalyst. *Fuel Process. Technol.* **2015**, *134*, 480–486. [[CrossRef](#)]
93. Sun, D.; Du, Y.; Wang, Z.; Zhang, J.; Li, Y.; Li, J.; Kou, L.; Li, C.; Li, J.; Feng, H.; et al. Effects of CaO Addition on Ni/CeO₂-ZrO₂-Al₂O₃ Coated Monolith Catalysts for Steam Reforming of N-Decane. *Int. J. Hydrogen Energy* **2020**, *45*, 16421–16431. [[CrossRef](#)]
94. Jayaprakash, S.; Dewangan, N.; Jangam, A.; Kawi, S. H₂S-Resistant CeO₂-NiO-MgO-Al₂O₃ LDH-Derived Catalysts for Steam Reforming of Toluene. *Fuel Process. Technol.* **2021**, *219*, 106871. [[CrossRef](#)]
95. Ashok, J.; Kawi, S. Low-Temperature Biomass Tar Model Reforming over Perovskite Materials with DBD Plasma: Role of Surface Oxygen Mobility. *Energy Convers. Manag.* **2021**, *248*, 114802. [[CrossRef](#)]
96. Chen, X.; Ma, X.; Peng, X. Effect of Lattice Oxygen in Ni-Fe/Bio-Char on Filamentous Coke Resistance during CO₂ Reforming of Tar. *Fuel* **2022**, *307*, 121878. [[CrossRef](#)]
97. Varvoutis, G.; Lykaki, M.; Stefa, S.; Binas, V.; Marnellos, G.E.; Konsolakis, M. Deciphering the Role of Ni Particle Size and Nickel-Ceria Interfacial Perimeter in the Low-Temperature CO₂ Methanation Reaction over Remarkably Active Ni/CeO₂ Nanorods. *Appl. Catal. B Environ.* **2021**, *297*, 120401. [[CrossRef](#)]
98. Varvoutis, G.; Karakoulia, S.A.; Lykaki, M.; Stefa, S.; Binas, V.; Marnellos, G.E.; Konsolakis, M. Support-Induced Modifications on the CO₂ Hydrogenation Performance of Ni/CeO₂: The Effect of ZnO Doping on CeO₂ Nanorods. *J. CO₂ Util.* **2022**, *61*, 102057. [[CrossRef](#)]
99. Lu, Y.; Li, S.; Guo, L. Hydrogen Production by Supercritical Water Gasification of Glucose with Ni/CeO₂/Al₂O₃: Effect of Ce Loading. *Fuel* **2013**, *103*, 193–199. [[CrossRef](#)]
100. de Caprariis, B.; Bracciale, M.P.; De Filippis, P.; Hernandez, A.D.; Petrullo, A.; Scarsella, M. Steam Reforming of Tar Model Compounds over Ni Supported on CeO₂ and Mayenite. *Can. J. Chem. Eng.* **2017**, *95*, 1745–1751. [[CrossRef](#)]
101. Xu, M.; Hu, H.; Yang, Y.; Huang, Y.; Xie, K.; Liu, H.; Li, X.; Yao, H.; Naruse, I. A Deep Insight into Carbon Conversion during Zhundong Coal Molten Salt Gasification. *Fuel* **2018**, *220*, 890–897. [[CrossRef](#)]
102. Zhou, L.; Li, L.; Wei, N.; Li, J.; Basset, J.M. Effect of NiAl₂O₄ Formation on Ni/Al₂O₃ Stability during Dry Reforming of Methane. *Chem. Cat. Chem.* **2015**, *7*, 2508–2516. [[CrossRef](#)]
103. Qiu, H.; Ran, J.; Huang, X.; Ou, Z.; Niu, J. Unrevealing the Influence That Preparation and Reaction Parameters Have on Ni/Al₂O₃ Catalysts for Dry Reforming of Methane. *Int. J. Hydrogen Energy* **2022**, *47*, 34066–34074. [[CrossRef](#)]
104. Norouzi, O.; Safari, F.; Jafarian, S.; Tavasoli, A.; Karimi, A. Hydrothermal Gasification Performance of Enteromorpha Intestinalis as an Algal Biomass for Hydrogen-Rich Gas Production Using Ru Promoted Fe-Ni/γ-Al₂O₃ Nanocatalysts. *Energy Convers. Manag.* **2017**, *141*, 63–71. [[CrossRef](#)]

105. Furusjö, E.; Ma, C.; Ji, X.; Carvalho, L.; Lundgren, J.; Wetterlund, E. Alkali Enhanced Biomass Gasification with in Situ S Capture and Novel Syngas Cleaning. Part 1: Gasifier Performance. *Energy* **2018**, *157*, 96–105. [[CrossRef](#)]
106. Chan, Y.H.; Syed Abdul Rahman, S.N.F.; Lahuri, H.M.; Khalid, A. Recent Progress on CO-Rich Syngas Production via CO₂ Gasification of Various Wastes: A Critical Review on Efficiency, Challenges and Outlook. *Environ. Pollut.* **2021**, *278*, 116843. [[CrossRef](#)]
107. Lampropoulos, A.; Binas, V.D.; Zouridi, L.; Athanasiou, C.; Montes-Morán, M.A.; Menéndez, J.A.; Konsolakis, M.; Marnellos, G.E. CO₂ Gasification Reactivity and Syngas Production of Greek Lignite Coal and Ex-Situ Produced Chars under Non-Isothermal and Isothermal Conditions: Structure-Performance Relationships. *Energies* **2022**, *15*, 679. [[CrossRef](#)]

Disclaimer/Publisher's Note: The statements, opinions and data contained in all publications are solely those of the individual author(s) and contributor(s) and not of MDPI and/or the editor(s). MDPI and/or the editor(s) disclaim responsibility for any injury to people or property resulting from any ideas, methods, instructions or products referred to in the content.